Supporting Information: Structure and defect identification at self-assembled islands of CO_2 using scanning probe microscopy

Oscar Custance,[*,†] Emiliano Ventura-Macias,[‡] Oleksandr Stetsovych,[¶] Carlos Romero-Muñiz,[§] Tomoko K. Shimizu,[‖] Pablo Pou,[‡,⊥] Masayuki Abe,[#] Hironobu Hayashi,[†] Tadakatsu Ohkubo,[†] Shigeki Kawai,[†] and Ruben Perez[*,‡,⊥]

†*National Institute for Materials Science (NIMS), 1-2-1 Sengen, Tsukuba, 305-0047, Ibaraki, Japan*

‡*Departamento de Física Teórica de la Materia Condensada, Universidad Autónoma de Madrid, 28049, Madrid, Spain*

¶*Institute of Physics of Czech Academy of Sciences, CukrovarnickÃą 10, Prague 6, 16200, Prague, Czech Republic*

§*Departamento de Física de la Materia Condensada, Universidad de Sevilla, P.O. Box 1065, 41080, Seville, Spain*

‖*Department of Applied Physics and Physico-Informatics, Faculty of Science and Technology, Keio University, 3-14-1 Hiyoshi, Kohoku-ku, Yokohama, 223-8522, Kanagawa, Japan*

⊥*Condensed Matter Physics Center(IFIMAC), Universidad Autónoma de Madrid, 28049, Madrid, Spain*

#*Graduate School of Engineering Science, Osaka University, 1-3 Machikaneyama, Toyonaka, 560-0043, Osaka, Japan*

E-mail: custance.oscar@nims.go.jp; ruben.perez@uam.es

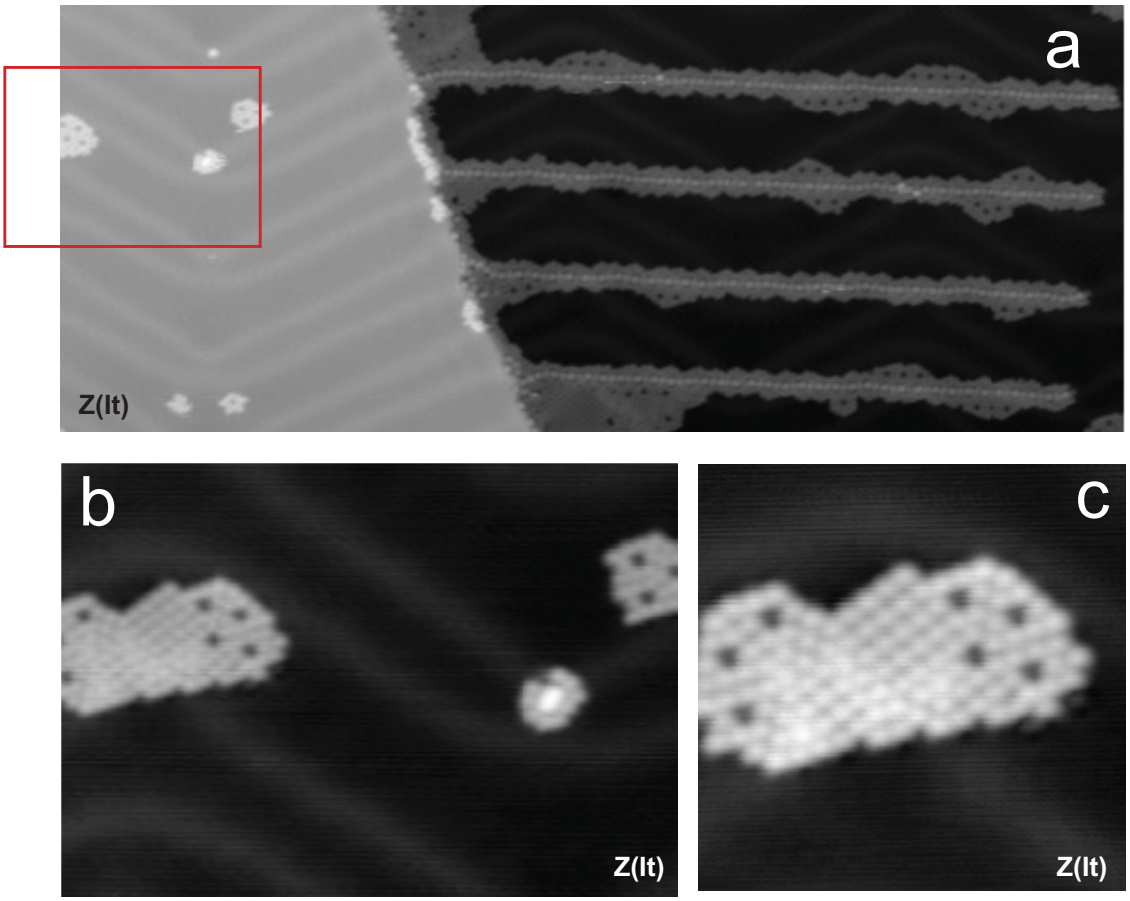

Figure S1: (a), Topographic STM image of an area of a Au(111) surface in which PDI, CO_2 and CO molecules were adsorbed; size (75×30) nm^2. The image shows the general morphology of the surface. The deposition of a small amount of PDI molecules on the Au(111) surface results in the formation of PDI–Au chains that grow from the lower part of a step edge towards the terraces. The red square highlights the location of the island displayed in figure 2 of the main text. (b), Topographic STM image of the region enclosed by the square in (a); size (18×12) nm^2. (c), Topographic STM image of the island displayed in figure 2 before starting the height-dependent series described in the text and shown in the movie accompany the supplementary information; size (8×8) nm^2. The sample bias voltage (V) and tunnelling current (I_T) set-point were: V= 150 mV and I_T= 5 pA for (a) and (b), and V= 70 mV and I_T= 5 pA for (c).

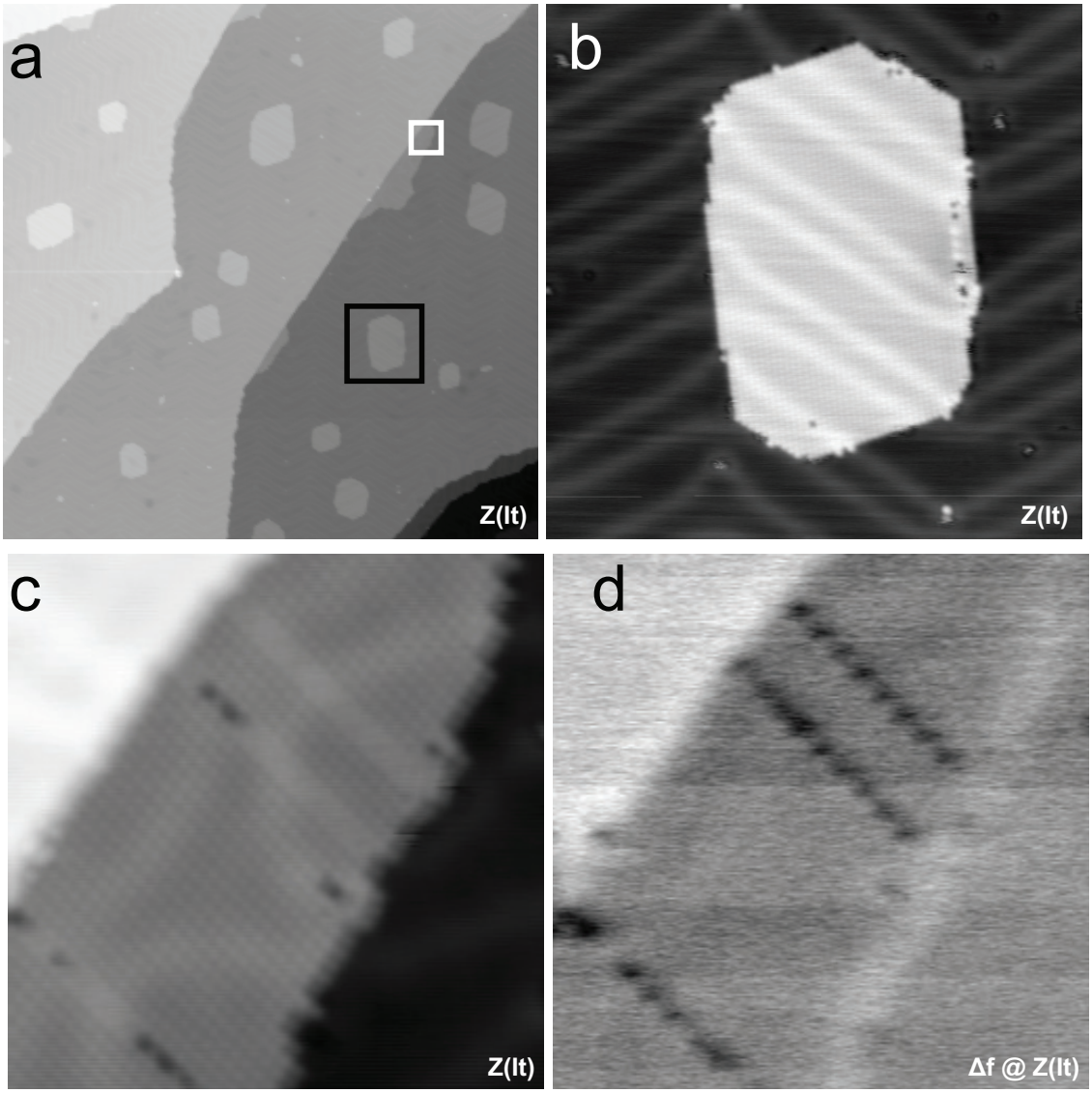

Figure S2: (a), Topographic STM image of a (250×250) nm^2 area of a Au(111) surface dosed with CO_2, and a small amount of CO molecules. In this sample, PDI molecules were not deposited on the surface. For the dosage level used in this study, CO_2 molecules nucleate preferentially at the middle of the terraces; nucleation at the lower terrace of step-edges is scarce. (b), Topographic STM image of the island of CO_2 molecules highlighted in (a) by a black square; size (35×35) nm^2. A single domain of molecules with an apparent rhombic arrangement dominates the island. On the right, some CO defects and a line of standing CO_2 molecules is observed due to the presence of nearby nucleation points. (c) and (d), Topographic STM image and simultaneously recorded AFM signal, respectively, of the surface area enclosed by the white square in (a); size (14×14) nm^2. CO defects and lines of standing CO_2 molecules are observed as the result of the coalescence of molecular domains with nucleation at different points of the step. Acquisition parameters for all images are: V= 500 mV and I_T= 5 pA.

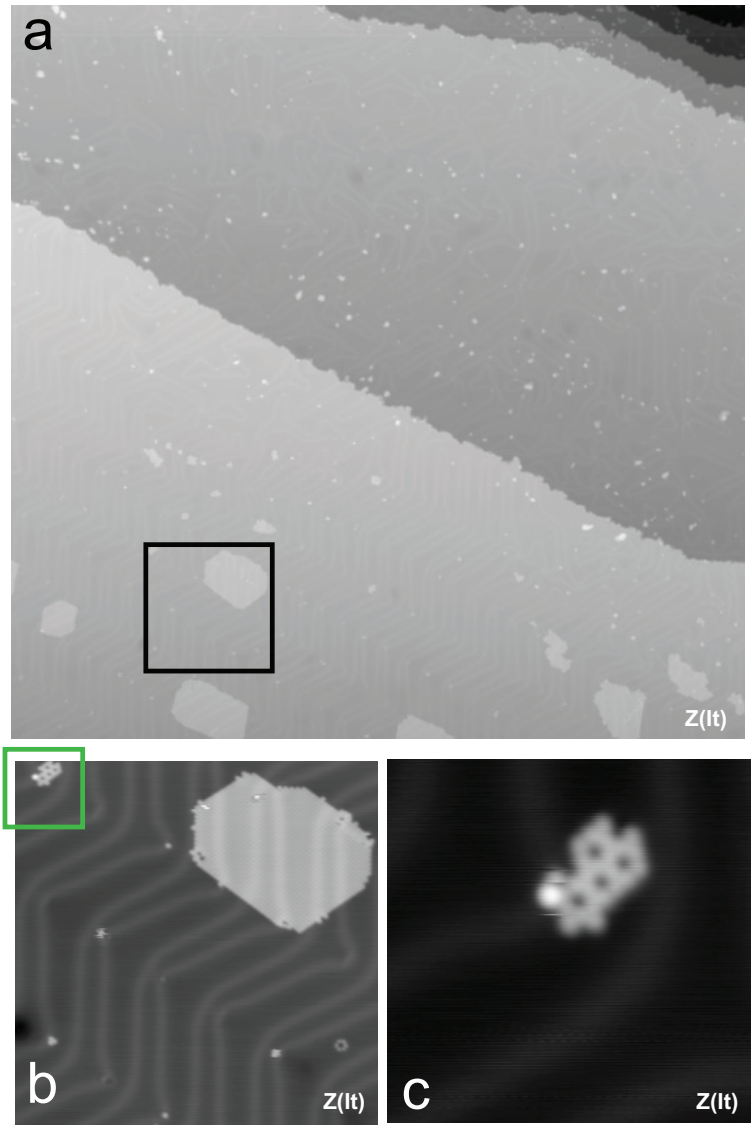

Figure S3: (a), Topographic STM image of a (250×250) nm^2 area of a Au(111) surface dosed with CO_2 and small amount of CO molecules. In this sample, PDI molecules were not deposited on the surface. (b), Topographic STM image of the region of interest highlighted by a square in (a), size (38×38) nm^2. Several defects in the single domain island of CO_2 locate over the elbows of the herringbone reconstruction of the Au(111) surface. The faint signal ascribed to a line of standing CO_2 is observed on the right side of the island. (c), Topographic STM image of the region enclosed by a (10×10) nm^2 square in (b) displaying an island of CO_2 nucleated around a small cluster of CO molecules (see Fig. S4 for more details). Acquisition parameters for all images are: V= 750 mV and I_T= 5 pA.

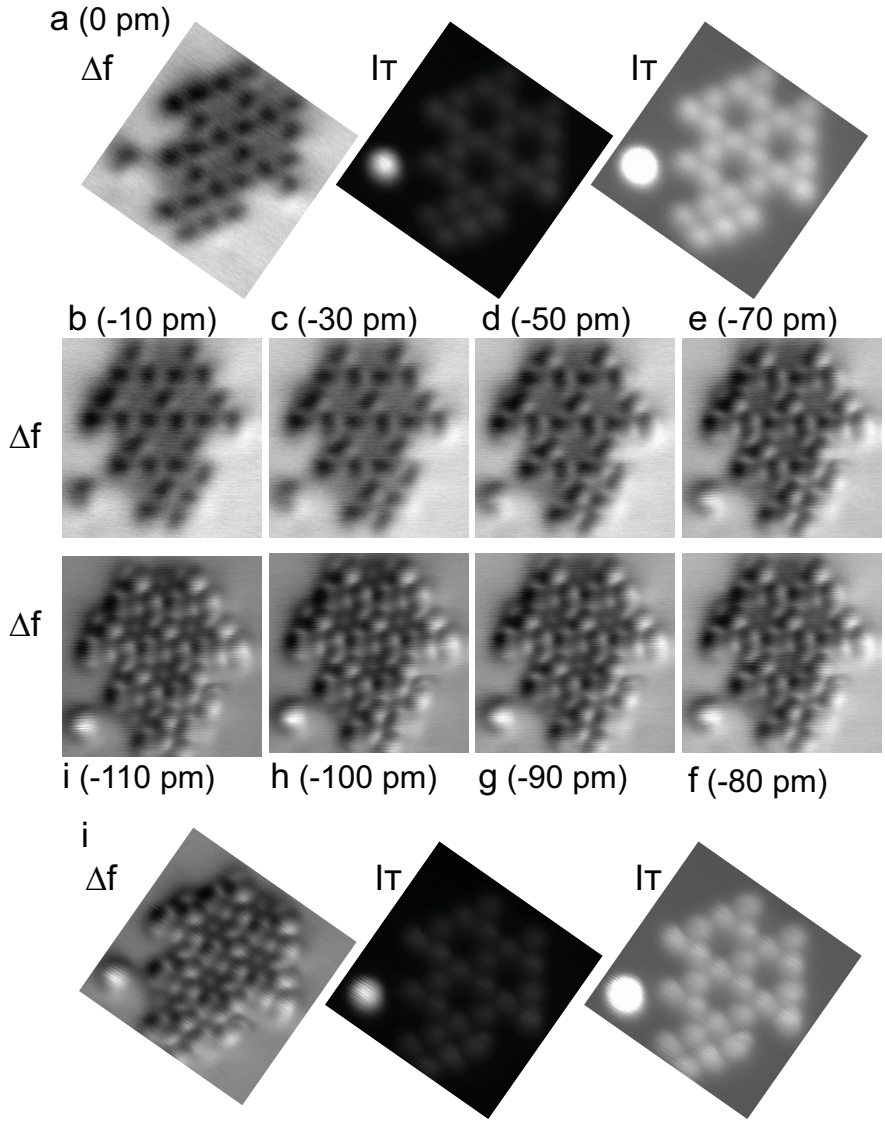

Figure S4: (a), Constant-height AFM (Δf) and STM (I_T) signals recorded over the island displayed in Fig. S3c. In this sample PDI molecules are absent from the surface. The STM image on the right was saturated over the cluster located at the elbow of the Au(111) herringbone reconstruction to enhance the contrast of the STM signal over the island. Some CO_2 molecules close to the elbow of the herringbone are missing with respect to the image in Fig. S3c due to dynamic processes that took place between the acquisition of both images (see Fig. S5 for details about dynamic processes). (b) to (i), Series of constant-height AFM images measured over the island shown in (a). The distance the probe was approached towards the surface with respect to the acquisition separation for (a) is displayed between brakes. (j) Constant-height AFM and STM signals recorded at the closest approach distance of the series, (i). A bias voltage of 10 mV was applied during the series acquisition. Image size for all images is (3×3) nm^2.

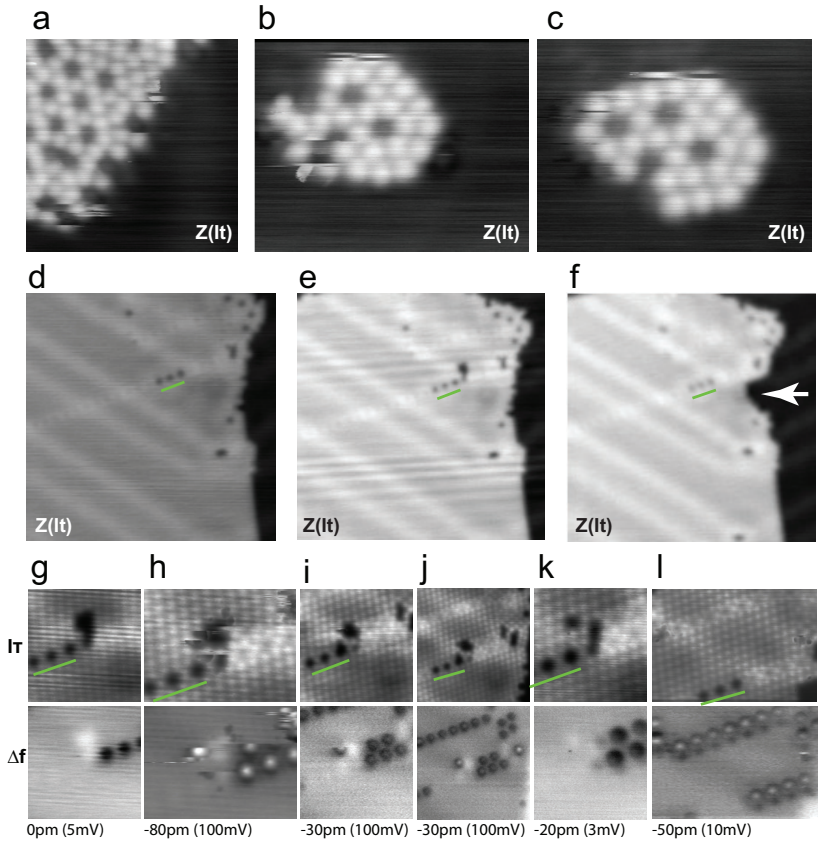

Figure S5: (a), Topographic STM image over an island of CO_2 showing diffusion of CO_2 molecules at the edge of the island. The fuzzy and striped protrusions along the edge are ascribed to mobile CO_2 molecules. Size is (3×3) nm^2, and acquisition parameters are: V= 250 mV and I_T= 5 pA. (b) and (c), Consecutive topographic STM images of an island of CO_2 molecules nucleating around a cluster of CO molecules. Diffusion of CO_2 is observed at the edges of the island, as well as the real-time formation of a windmill-like structure around the CO molecule at the upper left. Size and acquisition parameters are: (5×3.7) nm^2 for (b), (4.5×3.5) nm^2 for (c), and V= 250 mV and I_T= 5 pA for both. (d) to (l), Series of images acquired over an island of CO_2 molecules showing the creation of a hole at the CO_2 layer and its spontaneous refilling during imaging. In (d), the original area of the surface is presented. When zooming in over the area close to the three CO molecules marked with a green line, an unintentional interaction of the probe with the surface resulted in the formation of the hole visible in (e) by the removal of a few CO_2 molecules. After conditioning the probe far from the island, and adsorbing a CO at the apex, the series of constant-height simultaneously recorded STM and AFM images presented in (g) to (l) was recorded. During the acquisition of the series, CO_2 molecule were diffusing while scanning over the region until the hole in the layer was filled with CO_2 molecules (l) and (f). During the filling process, it is possible to observe the formation and disappearance of standing CO_2 molecules (h) and (i). The refilling process modified the morphology of the edge of the island, as pointed out by the arrow in (f). The position of the three CO defects in the series is highlighted by a green line over the STM images; at the range of probe-surface separations explored, the CO defects are not visible by the AFM. The approach distance from the imaging conditions in (g) and the applied voltage bias are displayed at the bottom of each set of images.

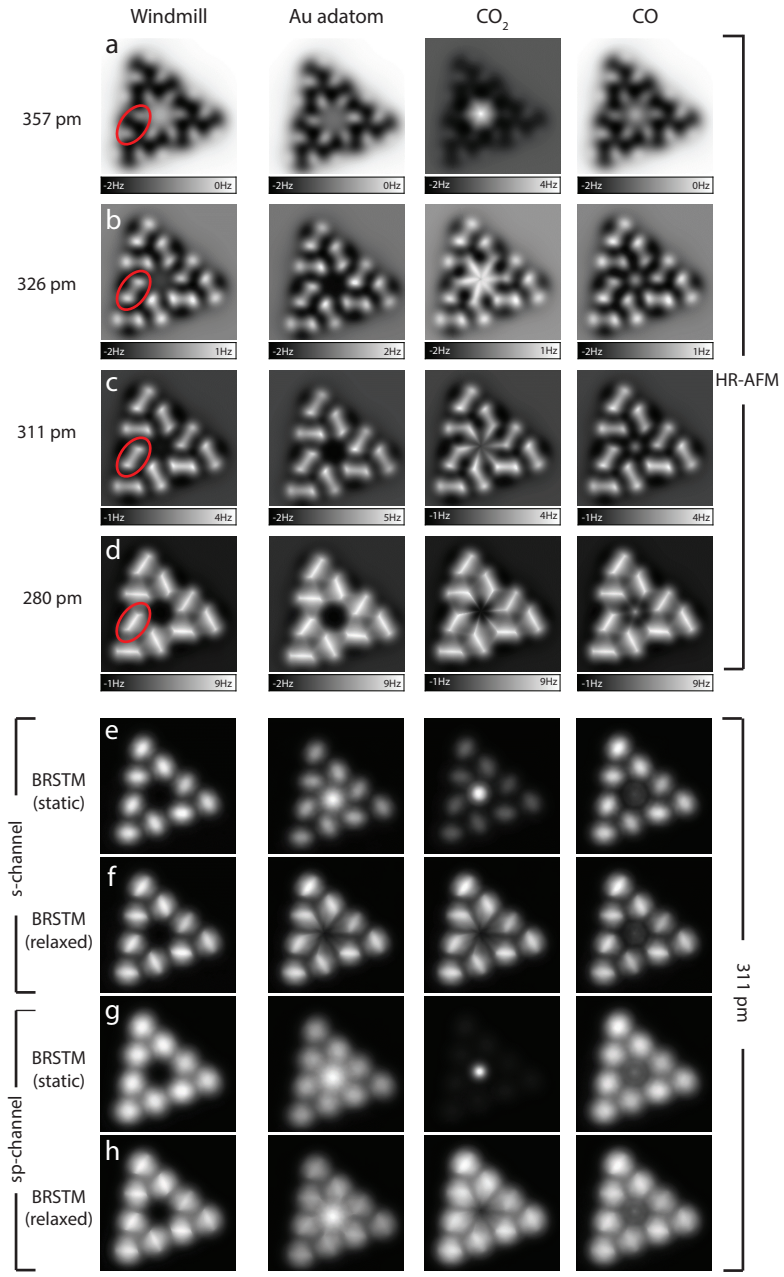

Figure S6: (a) to (d), AFM images for four representative probe-surface separations (357 pm, 326 pm, 311 pm, and 280 pm) using an oscillation amplitude of 70 pm are displayed. The red ovals in (a) to (d) mark the same CO_2 molecule of the windmill for comparison of contrast with the distance. (e) to (h), STM images for a 311 pm separation. The row of images labelled as *s–channel* in (e) and (f) are calculated considering only the contribution of the 5σ CO orbital to the tunnelling current. The row of images labelled as *sp–channel* in (g) and (h) take into account the contribution of both the 5σ and the $2\pi^*$ orbitals of the CO (represented by the s and the p_x, p_y orbital channels, see Methods). The rows displaying the label (*relaxed*) show images including the relaxation of the CO probe, in contrast to the images calculated assuming a static CO probe, labeled as (*static*). The distances are measured from the oxygen atom of the CO probe in a vertical position to the plane of the CO_2 layer. The defects follow the same order and labeling as in Fig. 3.

Text related to Figure S7.

To simulate the herringbone structure of the CO_2 molecules adsorbed on the Au(111) surface, we first considered a commensurate layer of CO_2 molecules over the unreconstructed Au(111) surface, following the stable rhombic configuration (a $2 \times \sqrt{3}$ unit cell) reported by Feng et al.[S1] In order to create a unit cell large enough to accommodate the defects, we increased the cell dimension from the original $2 \times \sqrt{3}$ unit cell (that includes two CO_2 molecules) to a $10 \times 5\sqrt{3}$ unit cell with 50 CO_2 molecules (see Table S1 for a description of each system).

We observed, however, that a small perturbation on the position of a single molecule in this large unit cell opens up a new solution for the system in which several molecules abandon their planar configuration and stand up to minimize the repulsion between the oxygen atoms. Thus, commensurate configurations seem to be unstable (at least up to the rather large sizes that we considered).

A stable solution is obtained when considering an island of CO_2 molecules instead. This island is created by removing molecules at the border of the cell, reducing the number of CO_2 molecules fitting in a $10 \times 5\sqrt{3}$ cell from 50 to 32 molecules. This distribution allows enough room in the plane parallel to the surface for the molecules to accommodate a slight repulsive interaction between the oxygen atoms upon inducing a small perturbation of the position of one molecule, so that all the molecules can relax back to their planar rhombic configuration.

The CO_2 molecules weakly interact with the gold substrate, and the configuration of the molecular layer is dominated by the intermolecular interaction of the oxygen lone pairs with the carbon atoms of adjacent molecules. This solution provides an adsorption energy of 301 meV/molecule and place the planar layer of CO_2 molecules 3.34 Å above the gold substrate with an average C–C nearest–neighbour distance of 4.17 Å. Column "Island/Au(111)" in Table S1 provides average values for the nearest-neighbor distance and the intermolecular angle together with the corresponding RMS.

Figure S7 provides more information on the distance and angle distributions and the

relative displacements of the molecules in the island relaxed configuration compared to their positions in the commensurate structure. The experimental values measured for the monolayer of CO_2 molecule trapped between the PDI-Au chains shown in Figs. 1 and 6 provide a nearest-neighbour distance between CO_2 molecules of 4.0 ± 0.2 Å and an angle between lines connecting nearest–neighbor molecules of $75.7 \pm 0.5°$. (Column "CO_2 ML (Exp)" in Table S1).

When attempting to calculate the defects, we also noticed that removing a CO_2 molecule from the layer to create a vacancy and replace it later on with a foreigner species does not reproduce the experimental findings. We found out that the creation of a windmill structure, due to either the presence of a foreigner species at the surface upon the nucleation of the CO_2 layer or due to the coalescence of different domains of CO_2 molecules, is key to host defects in the otherwise perfect molecular layer. Our DFT calculations confirm that the empty windmill structure as well as the ones hosting an Au adatom, a CO molecule and a standing CO_2 molecule are stable.

Table S1: The last two columns compare the structural parameters (lattice parameters a, b, nearest–neighbour distance (nn-d), and the angle (ϕ) between the molecular axis of the two CO_2 molecules) reported in ref. S1 (Column "Feng ML/Au(111)") with our DFT results (Column "ML/Au(111)"), see Methods in the main text for details on the calculations. The corresponding values for a free standing CO_2 monolayer in a herringbone configuration are shown in Column "f.s. CO_2 ML".

	CO_2 ML (Exp.)	Island/Au(111)	f.s. CO_2 ML	ML/Au(111)	Feng ML/Au(111)
a (Å)			6.22	5.80	5.79 (inferred)
b (Å)			5.02	5.02	4.95 (inferred)
nn-d (Å)	4.0±0.2	4.17±0.06	4.00	3.83	3.81
ϕ (Âž)	75.7±0.5	78.98±1.73	77.80	81.79	81.00

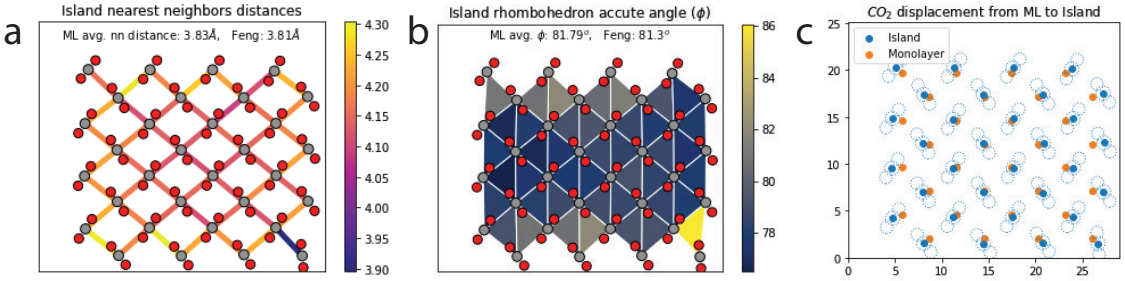

Figure S7: Detailed structural features of the CO_2 islands deposited on Au(111) reported in this work. (a) Nearest neighbors distancias, (b) rhomboedron accute angle (ϕ) and (c) the relative displacement of the molecules in the island with respect to a commensurate monolayer.

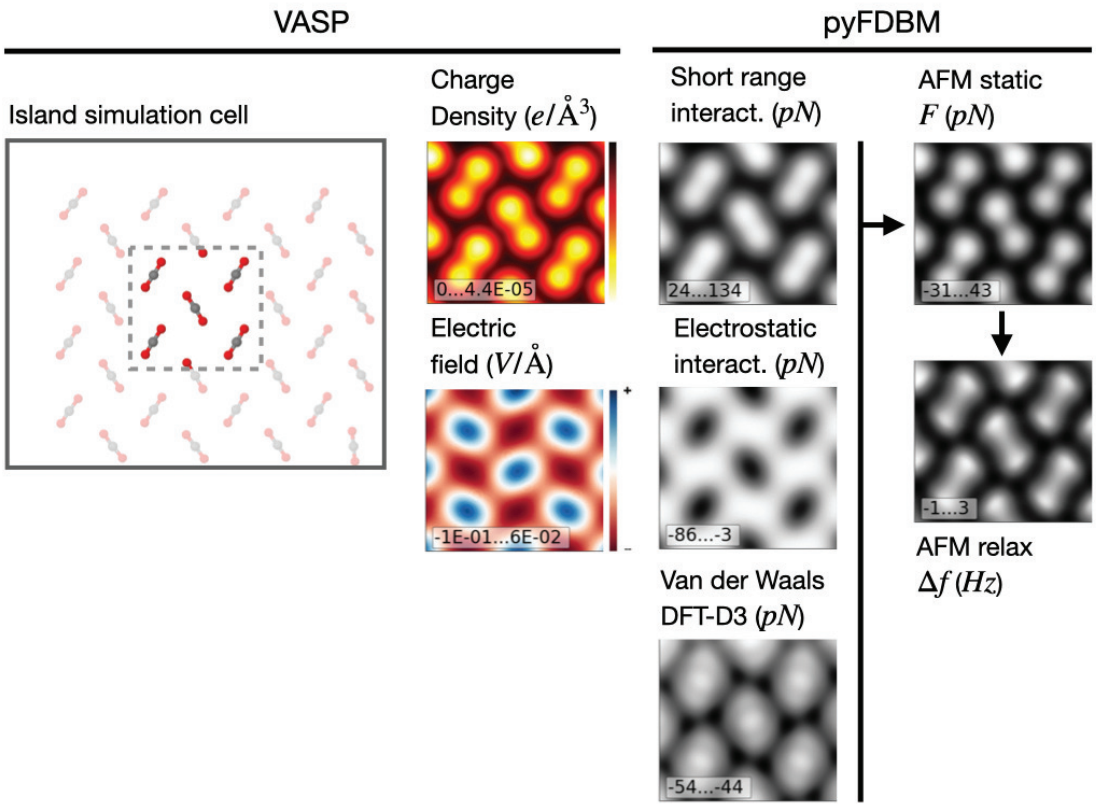

Figure S8: The application of the FDBM is illustrated with the case of CO_2 molecules arranged in a herringbone pattern in a CO_2 island adsorbed on Au(111) (see Fig. S7 for the structural details). The simulation cell and the DFT observables (charge density and electrostatic potential) obtained for this system are shown on the left. From these two observables, together with the charge density of the CO probe, the pyFDBM python code implementing the FDBM method, calculates the three relevant interactions (short–range, electrostatics and van der Waals)[S3] shown on the third column. The total sum is calculated (AFM static F, fourth column) and the lateral deflection of the CO probe in response to this total force is determined. The integration of the final forces along the CO trajectory during a cantilever oscillation provides access to the final frequency shift image (AFM Relax Δf, fourth column).[S4,S5] All force images obtained at a probe-sample distance of 3.12 Å. AFM frequency shift calculated with an oscillation amplitude of $A = 50$ pm for a distance of closest approach of 3.12 Å.

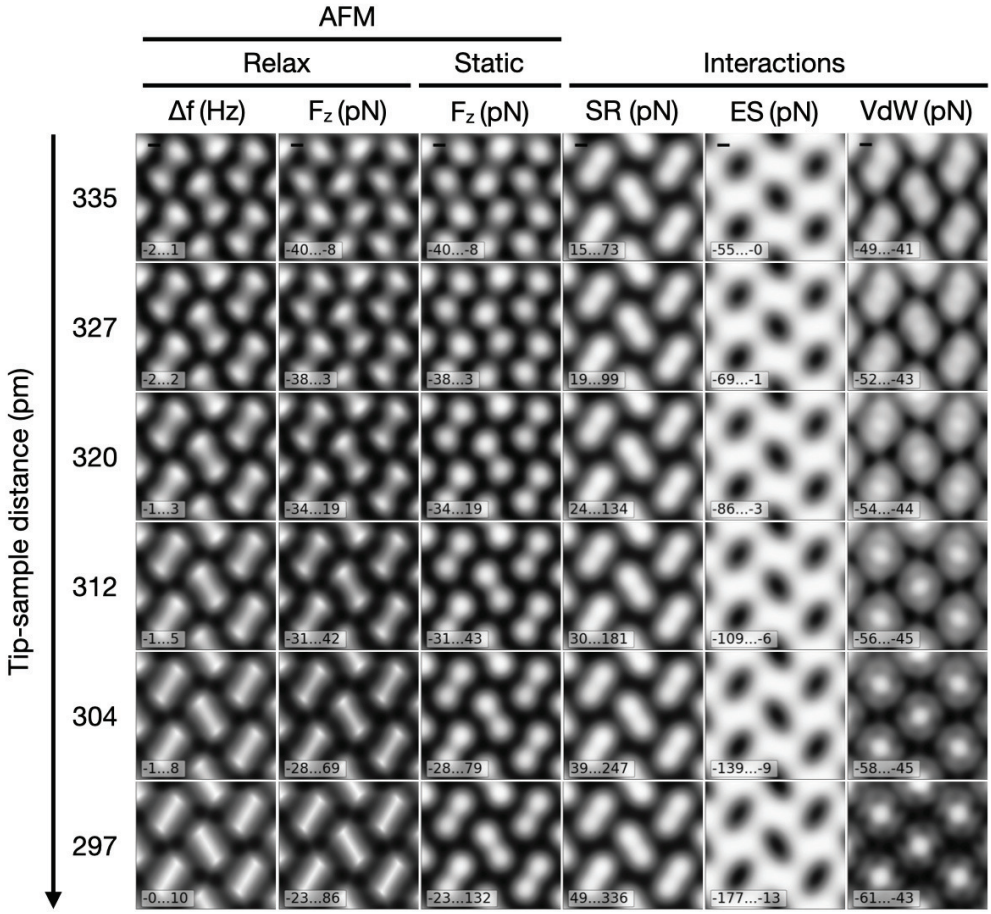

Figure S9: This close-up of a few molecules of a CO_2 island, arranged in a herringbone pattern, illustrates how the molecular contrast evolves from the dumbbell-like shape observed at relatively large probe–sample separation to the solid rod imaged at closer distances. This contrast evolution can be clearly seen over the CO_2 molecules composing the windmills in the experimental AFM images in Figs. 2c and 2d at the main text, and is very well reproduced by the theoretical Δf images calculated for an oscillation amplitude of $A = 50$ pm (panels in the left column, probe-sample distances of closest approach decrease from top to bottom). The rest of the columns (from the left, force after considering the relaxation of the CO_2 molecule, total static force (sum of the three interactions), short range, electrostatic, and van der Waals interactions) help to understand this contrast evolution. The AFM signal over the planar CO_2 is a balance between Pauli repulsion and electrostatic interaction, mostly determined by the electronic charge density distribution of the molecule. For large probe–sample distances, the charge density is dominated by the oxygen atoms, which are seen as the two lobes that produce the dumbbell shape. At closer separations, the electrostatic interaction over the carbon atoms becomes more apparent, developing into a faint feature that connects the two oxygen atoms of the CO_2. Upon further approach, this short-range interaction dominates the contrast, and the relaxation of the CO at the probe becomes significant, resulting in an image that displays each CO_2 molecule as a solid rod.

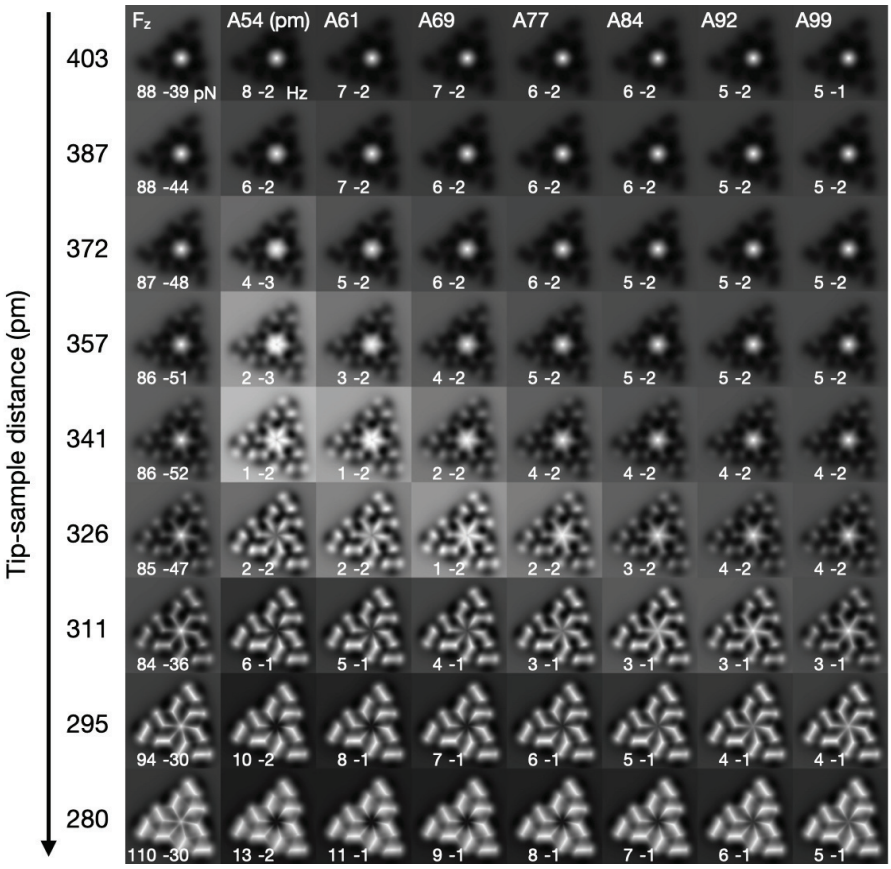

Figure S10: The appearance of a pinhole in the experimental AFM contrast over the standing CO_2 molecule at the closest probe-surface approach may suggest that the standing CO_2 molecule is quite mobile. Theoretical simulations show that the CO probe is much more mobile than the standing CO_2 molecule. Assuming that the position of the bottom oxygen atom is on the preferred adsorption site, we fixed it and let the standing CO_2 tilt inside the windmill. Then, we approached a CO probe attached to a Cu dimer, and relaxed both the standing CO_2 and the CO molecule at the probe using DFT calculations at each step. Results showed that the CO probe deflected $\sim$15° from a probe-sample separation of 300 pm to 270 pm, while in the same range the CO_2 only tilted $\sim$2°. Hence, the probe deflection has a larger impact in contrast to the CO_2 mobility. Moreover, the pinhole only appears in theoretical Δf images instead of force images, meaning that the frequency modulation operation plays a significant role in this case. In this figure we present images with different oscillation amplitudes, and show that the contrast disappears when using oscillation amplitudes smaller than 70 pm. The first column shows the force (F_z) image, which does not completely dissipates the standing CO_2 contrast. The other four columns show the frequency shift images with increasing amplitude, from 54 pm to 100 pm, where the smaller amplitudes evidence the missing standing CO_2 contrast in the experiments. The rows show an increasing probe-sample distance. Our study of frequency modulation measurements with a CO probe shows that this is a consequence of the change in force due to the probe deflection.[S5] Therefore, the disappearing contrast over the standing CO_2 is a combination of CO probe deflection and frequency modulation operation at amplitudes smaller than 70 pm.

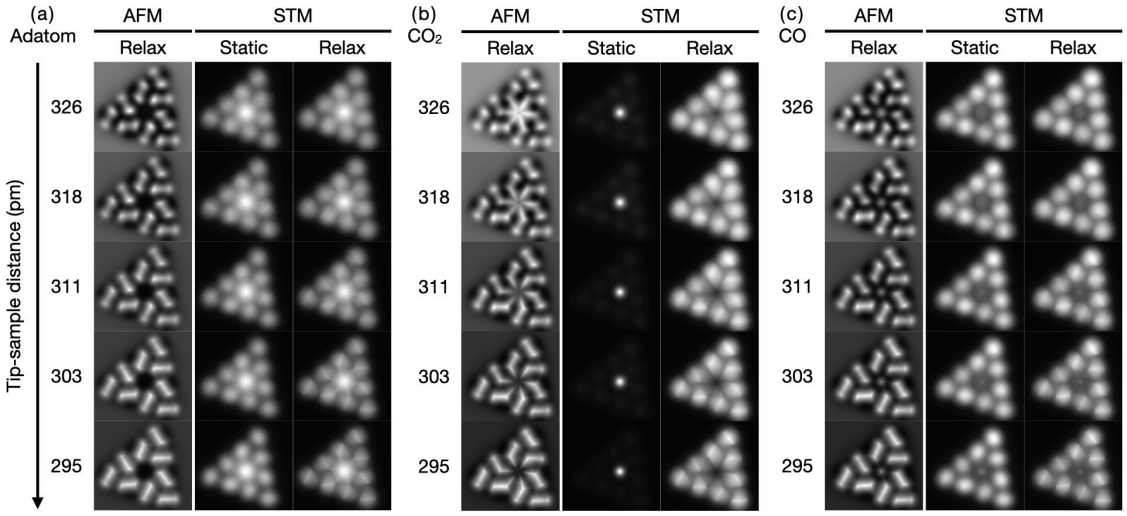

Figure S11: For each of the three defects (a) Windmill-adatom, (b) windmill-CO_2, and (c) windmill-CO, we provide for a range of probe heights, the corresponding AFM Δf image ("AFM Relax"), the STM image if the effect of the CO deflection is not taken into account ("STM static"), and the STM image when CO deflection is considered ("STM Relax"), with static (fixed-probe) and relaxed (deflected-probe) STM images. The AFM image has been calculated for an oscillation amplitude of 70 pm. The STM calculations include the contribution to the tunneling current of the 5σ and the $2\pi^*$ orbitals, represented by s and p_x, p_y orbital channels that contribute to the tunneling current through a sample wave function ψ with terms proportional to $|\psi|^2$ and to $|\partial\psi/\partial x|^2 + |\partial\psi/\partial y|^2$ respectively (see Methods in the main text). Both channels and the CO deflection are necessary to reproduce the contrast evolution of the bond-resolved STM images observed in the experiments (see Fig. 5 in the main text).

References

(S1) Feng, M., Sun, H., Zhao, J. & Petek, H. Self-Catalyzed Carbon Dioxide Adsorption by Metal-Organic Chains on Gold Surfaces. *ACS Nano* **8**, 8644–8652 (2014). URL https://doi.org/10.1021/nn5035026.

(S2) Feng, M. *et al.* Cooperative Chemisorption-Induced Physisorption of CO_2 Molecules by Metal-Organic Chains. *ACS Nano* **9**, 12124–12136 (2015). URL https://doi.org/10.1021/acsnano.5b05222.

(S3) Ellner, M., Pou, P. & Pérez, R. Molecular identification, bond order discrimination, and apparent intermolecular features in atomic force microscopy studied with a charge density based method. *ACS Nano* **13**, 786–795 (2019). URL https://doi.org/10.1021/acsnano.8b08209.

(S4) Zahl, P. *et al.* Hydrogen bonded trimesic acid networks on Cu(111) reveal how basic chemical properties are imprinted in HR-AFM images. *Nanoscale* **13**, 18473–18482 (2021). URL https://doi.org/10.1039/D1NR04471K.

(S5) Ventura-Macias, E., Romero-Muñiz, C., González-Sánchez, P., Pou, P. & Pérez, R. Are High Resolution Atomic Force Microscopy images proportional to the force gradient or the force maps? *Appl. Surf. Sci.* **634**, 157558 (2023). URL https://doi.org/10.1016/j.apsusc.2023.157558.